



Cite this: *Phys. Chem. Chem. Phys.*,
2016, 18, 26980

Infrared spectrum of the cold *ortho*-fluorinated protonated neurotransmitter 2-phenylethylamine: competition between $\text{NH}^+ \cdots \pi$ and $\text{NH}^+ \cdots \text{F}$ interactions†

Markus Schütz, Aude Bouchet and Otto Dopfer*

Halogenation of pharmaceutical molecules is a common tool to modify their physiological properties. The geometric, vibrational, and electronic properties of the *ortho*-fluorinated protonated neurotransmitter 2-phenylethylamine ($\text{oF-H}^+\text{PEA}$) are characterized by infrared photodissociation (IRPD) spectroscopy in the NH stretch range using the messenger technique and dispersion-corrected density functional theory calculations at the B3LYP-D3/aug-cc-pVTZ level to elucidate the drastic effect of site-specific *ortho*-fluorination. The IRPD spectra of cold $\text{oF-H}^+\text{PEA-Rg}$ dimers ($\text{Rg} = \text{Ne, Ar}$) are assigned to the most stable *gauche* conformer (Gf1) of $\text{oF-H}^+\text{PEA}$, which benefits from both $\text{NH}^+ \cdots \pi$ and $\text{NH}^+ \cdots \text{F}$ interactions. A minor contribution ($\sim 5\%$) of the slightly less stable Gf2 *gauche* conformer ($E_0 = +1.1 \text{ kJ mol}^{-1}$) is also identified. Comparison of $\text{oF-H}^+\text{PEA}$ with unsubstituted H^+PEA reveals a much stronger $\text{NH}^+ \cdots \pi$ interaction in H^+PEA resulting in a large red shift of the bonded NH stretch frequency. This behavior is confirmed by natural bond orbital (NBO) analysis and noncovalent interaction (NCI) calculations. The Rg ligand prefers a binding site at which it can maximize the interaction with the aromatic π electron system and the ammonium group. Although the intermolecular interactions with the Rg atoms can compete with the noncovalent intramolecular bonds, they induce only minor spectral shifts in the NH stretch range.

Received 26th August 2016,
Accepted 14th September 2016

DOI: 10.1039/c6cp05915e

www.rsc.org/pccp

1. Introduction

Fluorination of pharmaceutical compounds modulates physicochemical properties of bioactive molecules such as chemical reactivity, metabolic stability, protein–ligand interactions, binding mechanisms with enzymes or receptors, and transport and absorption characteristics of pharmaceuticals.^{1–9} 2-Phenylethylamine (PEA), with an aromatic ring and a flexible ethylamino side chain, represents the prototype of the large family of more complex aromatic ethylamino neurotransmitters, including dopamine and serotonin, and other psycho-active drugs such as amphetamines. Under physiological conditions, these neurotransmitters are usually protonated at the basic amino group of the side chain. Recently, we characterized the structural, vibrational, and energetic properties of a series of such protonated neurotransmitters (*e.g.*, histamine, dopamine, serotonin, (fluorinated) PEA, phenylalkylamines) by means of infrared multiphoton dissociation (IRMPD) in the fingerprint and NH stretch ranges in room-temperature ion traps.^{10–14} Although the

observed IRMPD spectra are consistent with the most stable conformer of each species determined by quantum chemical calculations, the contributions of higher energy conformers could not be completely ruled out in several cases, because of the limited spectral resolution of the room-temperature IRMPD spectra. Higher-resolution IR photodissociation (IRPD) spectra have been obtained for H^+PEA and its monohydrate by tagging the ions with rare gas atoms ($\text{Rg} = \text{Ne or Ar}$) in a cold supersonic plasma expansion.^{15,16} Tagging with weakly-bound Rg atoms lowers the temperature of the ions and the effective dissociation energy.^{17–27} This approach allows for recording single-photon IRPD spectra of cold ions, yielding higher spectral resolution and thus substantial improvement in the quality of the conformer assignment. Here, we apply this technique to determine the most stable conformers of *ortho*-fluorinated protonated PEA ($\text{oF-H}^+\text{PEA}$), by analyzing the IRPD spectra of cold $\text{oF-H}^+\text{PEA-Rg}$ dimers with $\text{Rg} = \text{Ne and Ar}$ in the NH stretch range.

In the following, we briefly summarize the current knowledge about H^+PEA and $\text{F-H}^+\text{PEA}$ relevant for the current work. Quantum chemical calculations reveal two conformers for H^+PEA (Fig. 1), namely the most stable folded *gauche* conformer (G), which is stabilized by a strong noncovalent intramolecular $\text{NH}^+ \cdots \pi$ (cation– π) interaction between the protonated amino group and the aromatic π -electron system of the phenyl ring, and the

Institut für Optik und Atomare Physik, Technische Universität Berlin,
Hardenbergstr. 36, D-10623 Berlin, Germany. E-mail: dopfer@physik.tu-berlin.de

† Electronic supplementary information (ESI) available. See DOI: 10.1039/c6cp05915e

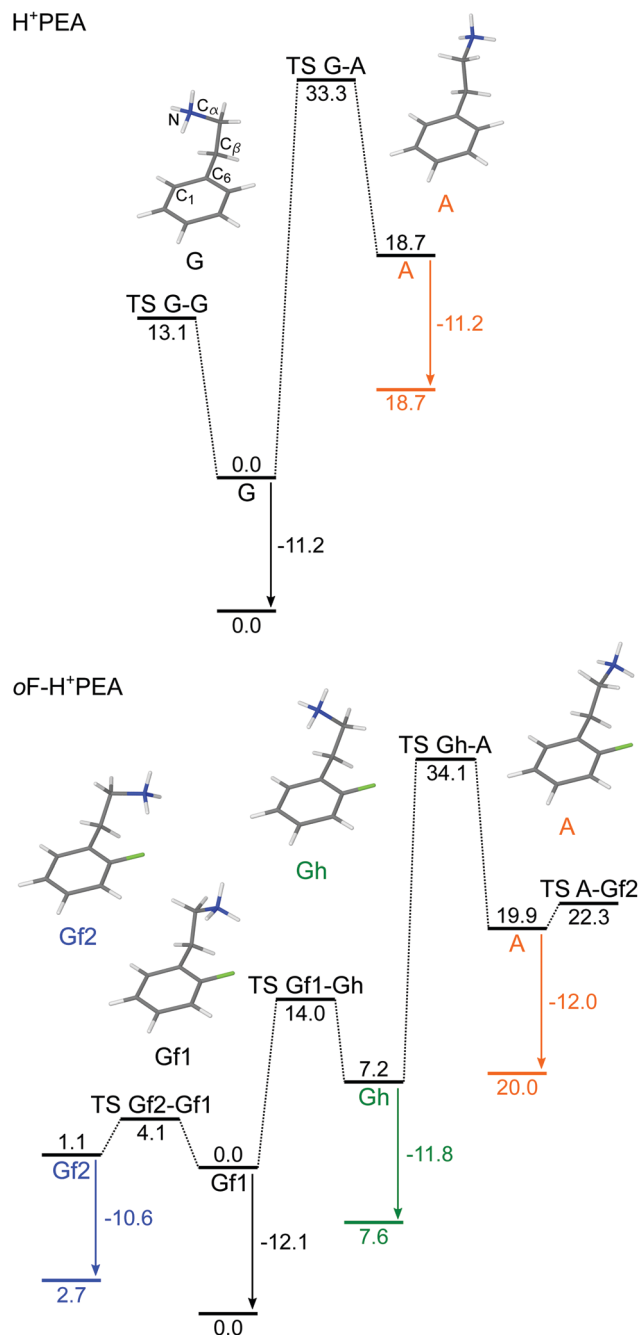


Fig. 1 Potential energy diagrams (E_0 in kJ mol^{-1}) of $o\text{F-H}^+\text{PEA}$ and H^+PEA , including nonequivalent minima and their connecting transition states. The arrows indicate the binding energy of Ar at the most stable binding site of the ($o\text{F-}$) H^+PEA conformers.

extended *anti* conformer (A), which is substantially higher in energy ($E_0 = +18.7 \text{ kJ mol}^{-1}$).¹⁵ Therefore, only the G conformer is detected in IRMPD spectra of H^+PEA ions stored in room-temperature ion traps¹³ and IRPD spectra of cold $\text{H}^+\text{PEA-Rg}_n$ clusters ($\text{Rg} = \text{Ne, Ar}; n \leq 3$) recorded in a supersonic expansion.¹⁵ Similarly, also the electronic photodissociation spectrum of H^+PEA was interpreted solely by the G conformer.²⁸ Protonation at the amino group causes conformational locking of neutral PEA, for which as many as four conformers are observed in cold molecular

beams.^{29,30} The effects of site-specific aromatic fluorine substitution of H^+PEA in *ortho*, *meta*, and *para* positions ($x\text{F-H}^+\text{PEA}$ with $x = o, m, p$) have been determined by IRMPD spectroscopy in the fingerprint range and dispersion-corrected density functional calculations at the B3LYP-D3/aug-cc-pVTZ level.¹⁴ $\text{H} \rightarrow \text{F}$ substitution has only a minor impact on the energy landscape and the properties of $m\text{F-H}^+\text{PEA}$ and $p\text{F-H}^+\text{PEA}$, because of the large distance between the F atom and the protonated ethylamino side chain. However, $\text{H} \rightarrow \text{F}$ substitution in *ortho* position drastically changes the energy landscape and the structures of the H^+PEA conformers because of the strong interaction between F and the nearby side chain (Fig. 1). In addition to the high-energy *anti* conformer (A, $E_0 = +19.9 \text{ kJ mol}^{-1}$), three low-energy *gauche* conformers with similar stabilities and low isomerization barriers are calculated for $o\text{F-H}^+\text{PEA}$, namely the Gf1, Gf2, and Gh conformers with $E_0 = 0, +1.1$, and $+7.2 \text{ kJ mol}^{-1}$, respectively. All *gauche* conformers merely differ by the configuration of the protonated side chain and the relative strengths of the competing $\text{NH}^+ \cdots \pi$ and $\text{NH}^+ \cdots \text{F}$ hydrogen bonds (H-bonds), which have been quantified in detail by use of the noncovalent interaction (NCI) approach.¹⁴ In the Gf1 and Gf2 conformers, the ammonium group is oriented toward the F atom, while in the Gh conformer it is pointing away from it. The experimental IRMPD spectra of all three $x\text{F-H}^+\text{PEA}$ isomers have been measured in the fingerprint range in a 300 K ion cyclotron resonance trap and mostly assigned to the respective *gauche* conformers. However, the insufficient spectral resolution of the IRMPD spectra ($\sim 30 \text{ cm}^{-1}$) and the similarity of the IR spectra predicted for all *gauche* conformers in the fingerprint range prevent an unambiguous assignment to one or more *gauche* conformers, as shown in Fig. S1 in ESI† for the case of $o\text{F-H}^+\text{PEA}$. On the other hand, the calculations predict clearly distinguishable IR spectra in the NH stretch range, which is very sensitive to the intramolecular H-bonds of the ammonium group and thus to the side chain conformation.¹⁴ To this end, we apply herein single-photon IRPD spectroscopy to cold $o\text{F-H}^+\text{PEA-Rg}$ dimers ($\text{Rg} = \text{Ne}$ and Ar) produced in a supersonic expansion using a narrow bandwidth IR laser (1 cm^{-1}) operating in the NH stretch range, an approach recently applied to $\text{H}^+\text{PEA-Rg}_n$ clusters.¹⁵ Previous comparison of the IRMPD spectrum of room-temperature H^+PEA with the IRPD spectra of cold $\text{H}^+\text{PEA-Rg}_n$ clusters clearly demonstrated the superior performance of IRPD over IRMPD in spectral resolution and reproduction of frequencies and relative intensities of fundamental transitions.¹⁵ The IRPD spectra of $o\text{F-H}^+\text{PEA-Rg}$ presented here allow for a clear-cut conformer assignment and provide for the first time invaluable experimental information of the drastic effects of *ortho*-fluorination on the $\text{NH}^+ \cdots \pi$ interaction in this prototypical protonated neurotransmitter, which are much more pronounced than those deduced for neutral PEA.^{31,32}

2. Experimental and computational details

The IRPD spectra of mass-selected $o\text{F-H}^+\text{PEA-Rg}$ clusters shown in Fig. 2 are recorded in a quadrupole tandem mass

spectrometer coupled to an electron impact ionization source and an octupole ion guide.^{22,33} Cold $oF-H^+PEA-Rg$ clusters are produced in a supersonic plasma expansion by electron and/or chemical ionization of $oF-PEA$ close to the nozzle orifice of a pulsed valve and subsequent clustering reactions in the high-pressure regime of the expansion. The expanding gas mixture is produced by passing Ne (7 bar) or Ar (8 bar) carrier gas through a reservoir filled with $oF-PEA$ (Sigma-Aldrich, 99%) and heated to 60 °C. Protonation of $oF-PEA$ occurs by self-protonation reactions and/or exothermic proton transfer from protonated water clusters resulting from water impurity in the gas inlet system. $oF-H^+PEA-Rg$ ions are selected by the first quadrupole mass spectrometer and deflected by a quadrupole bender into the octupole ion trap, where they are irradiated with IR photons in the 3000–3500 cm^{-1} range emitted from a tunable optical parametric oscillator (10 Hz, 2–5 mJ pulse⁻¹, 1 cm^{-1} bandwidth) pumped by a nanosecond Q-switched Nd:YAG laser. Calibration of the IR laser frequency to better than 1 cm^{-1} is accomplished by a wavemeter. The $oF-H^+PEA$ fragment ions produced by evaporation of the Rg ligands upon resonant IR excitation into vibrational modes of $oF-H^+PEA-Rg$ are selected by the second quadrupole and detected by a Daly detector as a function of the IR laser frequency to extract the IRPD spectrum. To separate metastable decay background from the laser-induced IRPD signal, the ion source is triggered at twice the laser frequency and signals from alternating triggers are subtracted. The IR laser power is monitored by a pyroelectric detector simultaneously with the IRPD spectra and found to be stable to within a factor two in the spectral range investigated. Although the IRPD spectra in Fig. 2 are not normalized for the laser intensity variations, the relative intensities of the transitions are believed to be accurate to within a factor of 2–3 arising mostly from variations in the overlap between the ion and laser beams. The widths of the transitions observed (~ 5 –10 cm^{-1} for Rg = Ne and ~ 10 –20 cm^{-1} for Rg = Ar) arise from a combination of the limited laser bandwidth, unresolved rotational substructure, and possible spectral congestion due to unresolved sequence hot bands involving low-frequency intermolecular modes and overlapping transitions of different isomers arising from various Rg binding sites.

Dispersion-corrected density functional theory calculations³⁴ are performed at the B3LYP-D3/aug-cc-pVTZ level to obtain geometric, vibrational, and energetic properties of $oF-H^+PEA$ and $oF-H^+PEA-Rg$. This theoretical level has previously been employed for $H^+PEA(-Rg)$ and yields satisfactory agreement with experimental data.¹⁵ Calculated harmonic frequencies are scaled with a factor of 0.9586 as previously derived for $H^+PEA(-Rg)$.¹⁵ If not stated otherwise, all reported energies are corrected for harmonic zero-point vibrational energy to yield relative energies (E_0) and intermolecular dissociation energies (D_0). The charge distribution is evaluated using the natural bond orbital (NBO) population analysis.³⁵ The noncovalent interaction (NCI) approach is employed to identify weak inter- and intramolecular noncovalent interactions.^{36,37} Visualization is obtained by plotting the reduced gradient of the electron density $s(\rho)$ against the electron density ρ oriented by the sign of the second

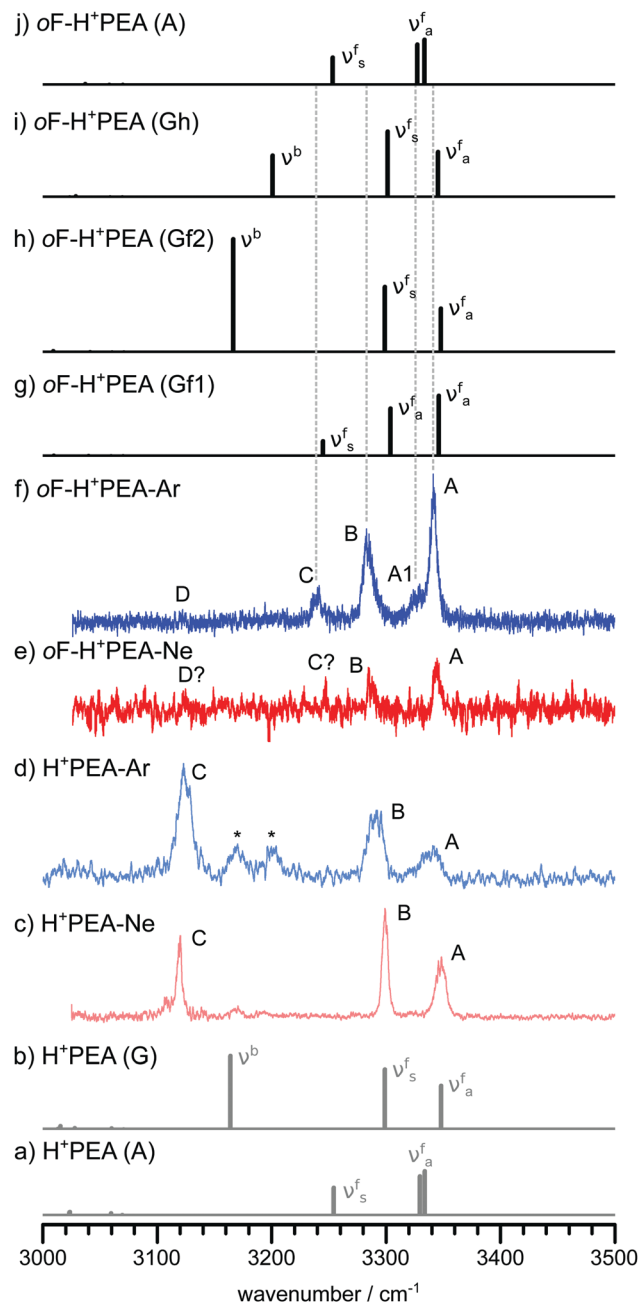


Fig. 2 IRPD spectra of $oF-H^+PEA-Ne$ (e) and $oF-H^+PEA-Ar$ (f) compared to linear IR absorption spectra calculated for all four conformers of $oF-H^+PEA$ (g–j). For comparison, the IRPD spectra of $H^+PEA-Ne$ (c) and $H^+PEA-Ar$ (d) and the linear IR absorption spectra calculated for the two H^+PEA conformers are reproduced as well (a and b).¹⁵ Frequencies calculated at the B3LYP-D3/aug-cc-pVTZ level are scaled by a factor of 0.9586. All computed spectra are drawn to the same scale. The positions and widths of the transitions observed (A–D) are listed in Table 1, along with their vibrational and conformer assignment. The bands marked by asterisks are assigned to overtone and combination bands.

eigenvalue λ_2 of the Hessian matrix, with $\rho^* = \rho \text{ sign}(\lambda_2)$. The ρ^* values (given in a.u.) provide a measure of the interaction strength. By use of a BGR color code covering the range $-1.25 < \rho^* < 1.25$ a.u., a representation of the isosurfaces with $s = 0.5$ a.u. is derived, in which blue surfaces correspond to attractive

interactions (negative λ_2), red surfaces to repulsive interactions (positive λ_2), and green surfaces ($\lambda_2 \approx 0$) to weak and delocalized dispersive interactions.

3. Results and discussion

The IRPD spectra of *o*F-H⁺PEA-Ne and *o*F-H⁺PEA-Ar are compared in Fig. 2 to the linear IR absorption spectra calculated for the four possible conformers of bare *o*F-H⁺PEA (Gf1, Gf2, Gh, A).¹⁴ For comparison, the corresponding IRPD spectra of H⁺PEA-Ne/Ar and the spectra calculated for the two nonequivalent H⁺PEA conformers (G, A) are reproduced as well.¹⁵ The positions and widths of the transitions observed are listed in Table 1 along with their vibrational and conformer assignments. As can be seen from the computed spectra in Fig. 2, the protonated amino group gives rise to three strongly IR active NH stretch fundamentals in the 3100–3400 cm^{−1} range. In the case of a C₃ symmetric environment, these three vibrations are composed of a higher-frequency degenerate antisymmetric e mode and a lower-frequency symmetric a mode.^{38–40} Reduction of symmetry and changes in force constants, *e.g.*, *via* hydrogen bonding, leads to a splitting of the e mode and frequency shifts of all three modes. In the case of the *anti* conformer of (*o*F)-H⁺PEA, the splitting of the e mode is small. The detection of more than three transitions in this spectral range in the experimental IRPD spectra is indicative of the presence of more than one conformer and/or isomers with different Rg binding sites and/or the presence of overtone and combination bands.

Before turning to the *o*F-H⁺PEA case, we briefly summarize the salient results for H⁺PEA.^{14,15} The experimental bands A, B, and C observed at 3348, 3299, and 3120 cm^{−1} for H⁺PEA-Ne are assigned to the two free antisymmetric and symmetric NH stretch modes (ν_a^f , ν_s^f) and the bound NH stretch mode (ν^b) involved in the NH⁺... π (cation- π) interaction of the *gauche* conformer (G), respectively. The two bands indicated by asterisks

are attributed to overtone and combination bands by comparison to anharmonic vibrational calculations. There is no sign of the less stable *anti* conformer (A) in the IRPD spectra. Calculations indicate that the frequency shifts induced by the weak interaction with the Ne tag ($D_0 < 3.85$ kJ mol^{−1}) are minor (<10 cm^{−1}). The overall appearance of the H⁺PEA-Ar spectrum is very similar to that of H⁺PEA-Ne with respect to both the positions and relative intensities of the transitions, with frequency shifts of less than 20 cm^{−1} arising from the stronger interaction with the Ar tag ($D_0 < 10.8$ kJ mol^{−1}).

The IRPD spectrum of *o*F-H⁺PEA-Ar is rather different from that of H⁺PEA-Ar, indicating that *ortho*-fluorination has a drastic impact on the preferred conformation of the flexible protonated ethylamino side chain. Three major bands A, B, and C are observed at 3341, 3283, and 3238 cm^{−1} and weaker transitions A1 and D are detected at 3329 and 3122 cm^{−1}, respectively. The *o*F-H⁺PEA-Ne spectrum exhibits a substantially lower signal-to-noise ratio than the *o*F-H⁺PEA-Ar spectrum but clearly reproduces the two strongest transitions A and B at 3344 and 3287 cm^{−1}, which are slightly blue-shifted (by 3–4 cm^{−1}) from the corresponding *o*F-H⁺PEA-Ar transitions. The detection of the transitions C and D in the *o*F-H⁺PEA-Ne spectrum is only tentative. Hence, we will utilize the richer *o*F-H⁺PEA-Ar spectrum for assigning the observed *o*F-H⁺PEA conformers by initial comparison to the IR spectra calculated for the four *o*F-H⁺PEA monomers in Fig. 2. The minor and subtle effects of Rg tagging will be considered in a second step.

Inspection of the IR spectra calculated for the four *o*F-H⁺PEA conformers (Gf1, Gf2, Gh, A) in Fig. 2 demonstrates that – in contrast to the fingerprint range (Fig. S1 in ESI†)¹⁴ – the NH stretch transitions are quite sensitive to the conformation of the ethylamino side chain and its various noncovalent intramolecular interactions, and thus allow for a clear-cut conformer assignment of the observed structures. As the structural and energetic properties calculated for the Gf1, Gf2, Gh, and A conformers with relative energies of $E_0 = 0, +1.1, +7.2$,

Table 1 Positions, widths (FWHM, in parentheses), and vibrational assignments of the transitions observed in the IRPD spectra of *o*F-H⁺PEA-Rg and H⁺PEA-Rg compared to frequencies and IR intensities (in km mol^{−1} in parentheses) of H⁺PEA, *o*F-H⁺PEA, and two *o*F-H⁺PEA(Gf1)-Rg isomers calculated at the B3LYP-D3/aug-cc-pVTZ level (Fig. 2 and 3)^a

	ν_a^f (cm ^{−1})		ν_a^f (cm ^{−1})		ν_s^f (cm ^{−1})		ν^b (cm ^{−1})	
H ⁺ PEA(G)	3348 (90)	A			3299 (123)	B	3164 (150)	C
H ⁺ PEA(A)	3333 (91)		3328 (81)		3254 (57)			
H ⁺ PEA-Ne (exp)	3348 (11)	A			3299 (6)	B	3120 (5)	C
H ⁺ PEA-Ar (exp)	3340 (20)	A			3291 (17)	B	3123 (15)	C
<i>o</i> F-H ⁺ PEA-Ne (exp)	3344 (6)	A	3287 (6)	B	3247 ^b	C	3125 ^b	D
<i>o</i> F-H ⁺ PEA-Ar (exp)	3341 (8)	A	3283 (11)	B	3238 (10)	C	3122	D
	3329 (~14)	A1						
<i>o</i> F-H ⁺ PEA(Gf1)	3346 (123)	A	3304 (97)	B	3245 (32)	C		
<i>o</i> F-H ⁺ PEA(Gf1)-Ar(i)	3347 (111)	A	3300 (133)	B	3239 (72)	C		
<i>o</i> F-H ⁺ PEA(Gf1)-Ar(iii)	3327 (204)	A1	3306 (193)	B	3244 (34)	C		
<i>o</i> F-H ⁺ PEA(Gf1)-Ne(i)	3347 (121)	A	3308 (112)	B	3251 (34)	C		
<i>o</i> F-H ⁺ PEA(Gf1)-Ne(iii)	3350 (156)	A	3308 (102)	B	3248 (28)	C		
<i>o</i> F-H ⁺ PEA(Gf2)	3348 (90)	A			3299 (134)	B	3166 (231)	D
<i>o</i> F-H ⁺ PEA(Gh)	3345 (93)				3301 (135)		3201 (86)	
<i>o</i> F-H ⁺ PEA(A)	3334 (93)		3327 (83)		3253 (57)			

^a Calculated frequencies are scaled by 0.9586. A complete list of calculated frequencies in the NH stretch range for all isomers of *o*F-H⁺PEA(Gf1)-Rg is available in Table S2 in ESI. Data for H⁺PEA(-Rg) are taken from ref. 15. ^b Tentative assignment.

and $+19.9 \text{ kJ mol}^{-1}$, respectively, are discussed in detail in ref. 14, we consider here only their N–H bond parameters summarized in Table S1 in ESI†. The A conformer has three N–H bonds with quite similar bond lengths (1.022 \AA), which give rise to three strongly coupled free NH stretch modes, namely two nearly degenerate high-frequency antisymmetric modes (ν_a^f) at 3334 and 3327 cm^{-1} and a low-frequency symmetric mode (ν_s^f) at 3253 cm^{-1} . The two more stable *gauche* conformers Gf2 and Gh exhibit two free N–H bonds with similar bond lengths (1.020 – 1.021 \AA), giving rise to coupled antisymmetric and symmetric NH stretch fundamentals (ν_a^f , ν_s^f) at around 3345 and 3300 cm^{-1} , respectively. In the Gh conformer, the third N–H bond is stretched by a weak $\text{NH}^+ \cdots \pi$ interaction to 1.028 \AA , corresponding to a largely red-shifted isolated bound NH stretch mode (ν^b) at 3201 cm^{-1} . In the Gf2 conformer, the third N–H bond is stretched by a stronger $\text{NH}^+ \cdots \text{F}$ interaction to 1.029 \AA , with an even lower-frequency bound NH stretch mode (ν^b) at 3166 cm^{-1} . Interestingly, the most stable Gf1 conformer benefits from weak $\text{NH}^+ \cdots \pi$ and $\text{NH}^+ \cdots \text{F}$ contacts, which give rise to three similar N–H bond lengths (1.020 – 1.024 \AA) and three largely coupled and roughly equally-spaced (nearly) free NH stretch fundamentals at $3346/3304 \text{ cm}^{-1}$ (ν_a^f) and 3245 cm^{-1} (ν_s^f).

Comparison of the IRPD spectra of the $\text{oF-H}^+\text{PEA-Rg}$ dimers with the IR spectra calculated for the four $\text{oF-H}^+\text{PEA}$ conformers in Fig. 2 suggests an immediate assignment of the most prominent bands A, B, and C to the three NH stretch fundamentals (ν_a^f , ν_s^f , ν^b) of the most stable Gf1 conformer. The very weak but clearly discernible band D in the $\text{oF-H}^+\text{PEA-Ar}$ spectrum is an unambiguous fingerprint of the minor presence of the second most stable Gf2 conformer (ν^b). Neglecting effects of Ar complexation, the abundance ratio of the Gf2 and Gf1 conformers can be roughly estimated as $\sim 5\%$ from the ratio of the integrated band intensities of band D and bands A–C, corrected for variations in the laser intensity and the calculated IR cross sections. The small population of the Gf2 conformer with relative energy of only $E_0 = +1.1 \text{ kJ mol}^{-1}$ compared to the Gf1 global minimum is indicative of the low cluster ion temperature achieved in the supersonic plasma expansion. The free NH stretch bands of Gf2 overlap with those of the much more abundant Gf1 conformer. As will be shown below, the band A1 observed only in the $\text{oF-H}^+\text{PEA-Ar}$ spectrum most likely arises from $\text{oF-H}^+\text{PEA(Gf1)-Ar}$ isomers with an Ar binding site producing a noticeable red shift from band A. The abundance of the Gh conformer is below the detection limit because its bound NH stretch transition predicted at $\nu^b = 3201 \text{ cm}^{-1}$ is absent in the IRPD spectra. This result is in line with its relative energy of $E_0 = +7.2 \text{ kJ mol}^{-1}$. Although the spectrum predicted for the A conformer of $\text{oF-H}^+\text{PEA}$ partly overlaps with the measured spectrum, its abundance can also be excluded for energetic reasons ($E_0 = +19.9 \text{ kJ mol}^{-1}$) and by analogy to the H^+PEA case.

In the following, we turn our attention toward the effects of Rg tagging on the structures, energetics, and IR spectra of the $\text{oF-H}^+\text{PEA}$ conformers. As the Gh and A conformers are experimentally not detected, we focus mostly on the predominant Gf1 conformer. Fig. 3 summarizes the six major binding sites and binding energies of the Rg atoms for Rg = Ar and Ne around the

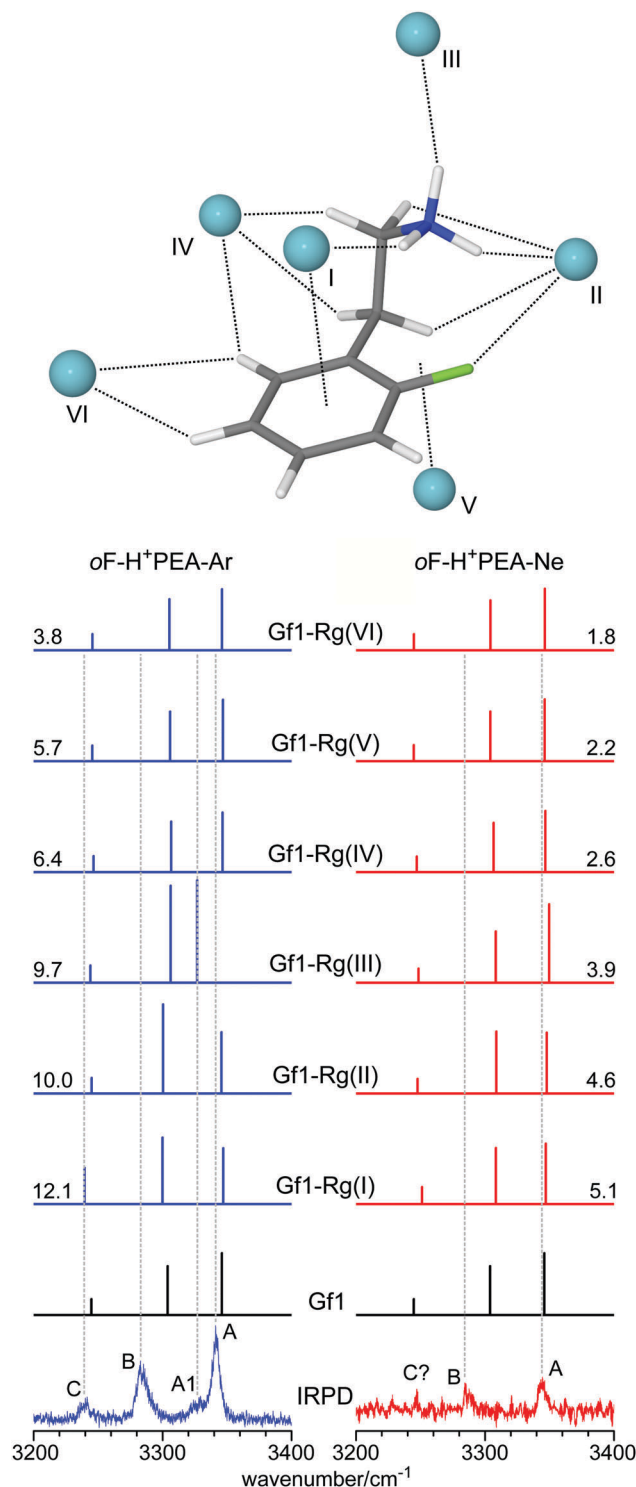


Fig. 3 IRPD spectra (bottom) of $\text{oF-H}^+\text{PEA-Ar}$ (left) and $\text{oF-H}^+\text{PEA-Ne}$ (right) compared to linear IR stick absorption spectra of the most stable Gf1 conformer of $\text{oF-H}^+\text{PEA}$ and its Rg-tagged ions for the six most stable Rg binding motifs indicated in the structure (B3LYP/aug-cc-pVTZ level). Binding energies (D_0) are given in kJ mol^{-1} .

Gf1 ion (I–VI), along with their predicted IR spectra (Table S2 in ESI†) and the measured IRPD spectra. The binding motifs and energetic order of the Gf1–Rg isomers are the same for both Rg atoms.

In the most favorable binding site I, the Rg atom interacts with the aromatic π -electron system *via* dispersion forces and one of the protons of the ammonium group *via* a $\text{NH}^+ \cdots \text{Ar}$ H-bond, leading to binding energies of $D_0 = 12.1$ and 5.1 kJ mol^{-1} for Rg = Ar and Ne, respectively. In the slightly less stable binding motif II, the Rg atom interacts with the F atom, one NH proton, and both CH_2 groups, with $D_0 = 10.0$ (Ar) and 4.6 (Ne) kJ mol^{-1} . Binding site III is mostly characterized by a $\text{NH}^+ \cdots \text{Rg}$ interaction along with a weak $\text{C}_\alpha\text{H}_2$ contact and $D_0 = 9.7$ (Ar) and 3.9 (Ne) kJ mol^{-1} . The remaining isomers IV–VI are substantially less stable, with $D_0 \leq 6.4$ (Ar) and 2.6 (Ne) kJ mol^{-1} , because the Rg atoms interact merely with aliphatic and/or aromatic $\text{CH}_{(2)}$ protons. The binding energies of Ar with the three less stable Gf2, Gh, and A conformers are listed in Table S3 in ESI†. Interestingly, all efforts to locate a Gf2–Rg(I) isomer failed, and all optimizations converged toward the Gf1–Rg(I) isomer, indicating a Rg-induced conformational isomerisation reaction ($\text{Gf2} \rightarrow \text{Gf1}$). Thus, position II is the most stable Rg binding site for Gf2, and this result may to some extent also contribute to the low abundance of this conformer in the $\text{oF-H}^+\text{PEA-Ar}$ spectrum.

Because of the relatively weak interaction of Ne with $\text{oF-H}^+\text{PEA(Gf1)}$ ($D_0 = 1.8\text{--}5.1 \text{ kJ mol}^{-1}$), the perturbation by tagging is small. As a consequence, the predicted IR spectra of all $\text{oF-H}^+\text{PEA(Gf1)-Ne}$ isomers are the same within experimental resolution and reflect the one of the untagged ion with respect to frequency ($\Delta\nu_{\text{NH}} \leq 6 \text{ cm}^{-1}$) and IR intensity ($\Delta I_{\text{NH}} < 30\%$) to high accuracy (Fig. 3 and Table S2 in ESI†). As a result, the preferred Ne binding site can not be inferred from the experimental IRPD spectrum. The prominent bands A and B observed at 3344 and 3287 cm^{-1} in the IRPD spectrum of $\text{oF-H}^+\text{PEA-Ne}$ are red-shifted by 2 and 17 cm^{-1} compared to the two ν_{a} fundamentals calculated as 3346 and 3304 cm^{-1} for bare $\text{oF-H}^+\text{PEA(Gf1)}$. Tagging with Ar affects the transitions slightly more because of its stronger interaction ($D_0 = 3.8\text{--}12.1 \text{ kJ mol}^{-1}$). For isomers I–II and IV–VI, the effects are again below or comparable to the experimental spectral resolution, with $\Delta\nu_{\text{NH}} \leq 6 \text{ cm}^{-1}$ and $\Delta I_{\text{NH}} < 125\%$ (Fig. 3 and Table S2 in ESI†). The only exception is isomer III, for which the highest-frequency free NH stretch band is red-shifted by 19 cm^{-1} because of the formation of a relatively strong $\text{NH}^+ \cdots \text{Ar}$ H-bond. Hence, the bands A, B, and C observed at 3341 , 3283 and 3238 cm^{-1} in the IRPD spectrum of $\text{oF-H}^+\text{PEA-Ar}$ are mostly assigned to the three free NH stretch fundamentals of isomer I (and possibly II) of $\text{oF-H}^+\text{PEA(Gf1)-Ar}$ predicted at

3347 , 3300 , and 3239 cm^{-1} , with deviations of -6 , -17 , and -1 cm^{-1} , respectively. The satellite transition A1 measured at 3329 cm^{-1} is currently interpreted as Ar-bound NH stretch of isomer III predicted at 3327 cm^{-1} , with an estimated abundance of roughly 20% compared to isomers I and II resulting from the ratio of the integrated band intensities of bands A and A1 corrected for the calculated IR cross sections.

Rg tagging with Ar and Ne leaves the conformational structure of $\text{oF-H}^+\text{PEA(Gf1)}$ nearly unchanged (Table 2). Relevant dihedral angles describing the side chain conformation (τ_1 and τ_2) deviate by less than 1.2° for the relevant I and III binding sites of the Rg atom. From this result, one can conclude that the intermolecular interactions of the Rg atoms do not affect much the noncovalent intramolecular bonds in $\text{oF-H}^+\text{PEA(Gf1)}$ and that they can be considered separately.

Analysis of the NBO charge distribution of $\text{oF-H}^+\text{PEA(Gf1)}$ and its most stable $\text{oF-H}^+\text{PEA(Gf1)-Rg(I)}$ dimer demonstrates only minor charge rearrangement by Rg tagging. As noted previously,^{13–16} the charge of the excess proton is mostly located on the side chain ($>930 \text{ me}$) with a major part on the ammonium group ($\approx 650 \text{ me}$). Upon Rg tagging at binding site I, only a small amount of the positive charge is transferred to the Rg atom (10 and 3 me for Ar and Ne, respectively), mainly shifted from the ammonium nitrogen atom (-7 and -3 me). The noncovalent inter- and intramolecular interactions occurring in $\text{H}^+\text{PEA(G)}$, $\text{oF-H}^+\text{PEA(Gf1)}$, and their most stable Ar dimers (isomer I) are quantified by NCI calculations (Fig. 4 and Table 3). Comparison of the 2D plots of $\text{oF-H}^+\text{PEA(Gf1)}$ and $\text{oF-H}^+\text{PEA(Gf1)-Ar(I)}$ reveals the same noncovalent intramolecular interactions with nearly similar strengths. The intramolecular $\text{NH}^+ \cdots \pi$ interaction in isolated $\text{oF-H}^+\text{PEA(Gf1)}$ ($R_{\text{NH} \cdots \pi} = 3.26 \text{ \AA}$, $\rho^* = -0.010 \text{ a.u.}$) gets slightly weaker in the Ar-tagged dimer ($R_{\text{NH} \cdots \pi} = 3.30 \text{ \AA}$, $\rho^* = -0.009 \text{ a.u.}$), because the Ar atom slightly pushes the side chain away from the aromatic ring. At the same time, the intramolecular $\text{NH}^+ \cdots \text{F}$ interaction ($R_{\text{NH} \cdots \text{F}} = 2.28 \text{ \AA}$, $\rho^* = -0.013 \text{ a.u.}$) becomes slightly stronger upon Ar tagging ($R_{\text{NH} \cdots \text{F}} = 2.24 \text{ \AA}$, $\rho^* = -0.013 \text{ a.u.}$). Additional intermolecular interactions of the Ar tag are the relatively strong $\text{NH}^+ \cdots \text{Ar}$ H-bond ($R_{\text{NH} \cdots \text{Ar}} = 2.54 \text{ \AA}$, $\rho^* = -0.010 \text{ a.u.}$) and the weaker delocalized dispersive $\text{Ar} \cdots \pi$ interaction ($R_{\text{Ar} \cdots \pi} = 3.58 \text{ \AA}$, $\rho^* = -0.004 \text{ a.u.}$). The intermolecular $\text{NH}^+ \cdots \text{Ar}$ bond is somewhat weaker than the intramolecular $\text{NH}^+ \cdots \text{F}$ and $\text{C}_\beta\text{H} \cdots \text{F}$ interactions ($\rho^* = -0.011 \text{ a.u.}$) because F has a better electron donor character than Ar. Interestingly, this intermolecular interaction is slightly stronger than the intramolecular

Table 2 Selected bond lengths ($R_{\text{NH} \cdots \pi}$, $R_{\text{NH} \cdots \text{F}}$, $R_{\text{Rg} \cdots \pi}$, $R_{\text{NH} \cdots \text{Rg}}$), dihedral angles τ_1 ($\text{C}_1\text{C}_6\text{C}_\beta\text{C}_\alpha$) and τ_2 ($\text{C}_6\text{C}_\beta\text{C}_\alpha\text{N}$), and zero-point corrected relative energies (E_0) and binding energies (D_0) of $\text{oF-H}^+\text{PEA(Gf1)}$ and two representative $\text{oF-H}^+\text{PEA(Gf1)-Rg}$ isomers calculated at the B3LYP-D3/aug-cc-pVTZ level

	$R_{\text{NH} \cdots \pi}^a/\text{\AA}$	$R_{\text{NH} \cdots \text{F}}^b/\text{\AA}$	$R_{\text{Rg} \cdots \pi}^a/\text{\AA}$	$R_{\text{NH} \cdots \text{Rg}}^b/\text{\AA}$	$\tau_1/^\circ$	$\tau_2/^\circ$	$E_0/\text{kJ mol}^{-1}$	D_0/cm^{-1}
$\text{oF-H}^+\text{PEA(Gf1)}$	3.26	2.275	—	—	95.6	55.2		
$\text{oF-H}^+\text{PEA(Gf1)-Ar(I)}$	3.30	2.243	3.58	2.538	95.2	55.3	0.0	1015
$\text{oF-H}^+\text{PEA(Gf1)-Ar(III)}$	3.28	2.311	—	2.497	95.8	56.3	2.4	814
$\text{oF-H}^+\text{PEA(Gf1)-Ne(I)}$	3.26	2.274	3.33	2.277	95.3	55.6	0.0	427
$\text{oF-H}^+\text{PEA(Gf1)-Ne(III)}$	3.27	2.311	—	2.262	95.6	56.2	1.3	323

^a Distance to the center of the aromatic ring. ^b Shortest $\text{NH}^+ \cdots \text{F}$ or $\text{NH}^+ \cdots \text{Rg}$ distance.

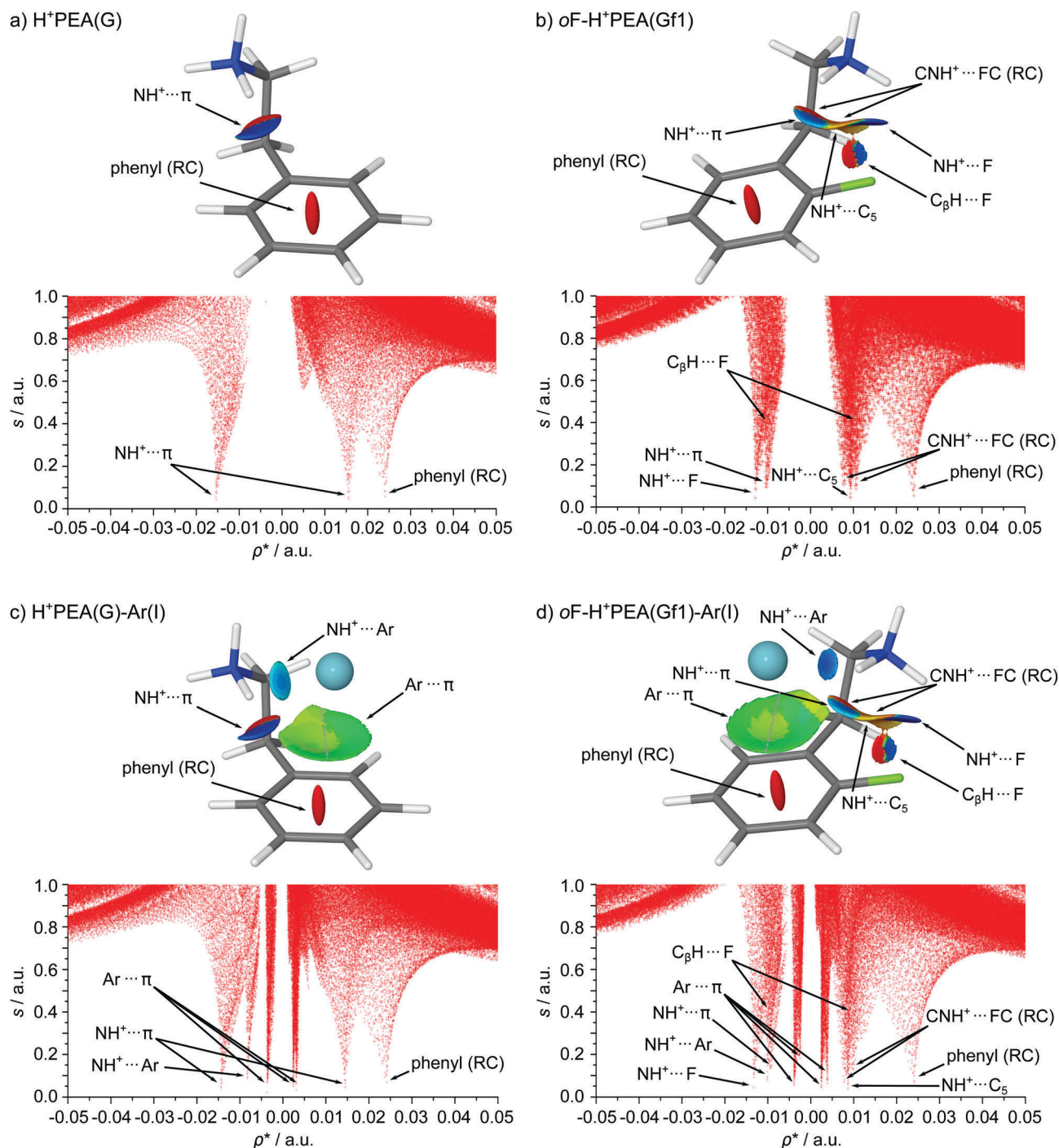


Fig. 4 Plots of the reduced gradient $s(\rho^*)$ as a function of the electron density ρ^* ($=\rho \text{ sign}(\lambda_2)$) and the corresponding NCI isosurfaces with a cutoff at $s = 0.5$ and a BGR color scheme range of -1.25 to 1.25 for (a) $H^+PEA(G)$, (b) $oF-H^+PEA(Gf1)$, (c) $H^+PEA(G)-Ar(I)$, and (d) $oF-H^+PEA(Gf1)-Ar(I)$. RC denotes ring closure. Table 3 lists the positions of ρ^* for minima in $s(\rho^*)$.

$NH^+ \cdots \pi$ interaction. Moreover, the $Ar \cdots \pi$ interaction is divided into two parts (indicated by the dotted line in Fig. 4d), where the stronger one ($\rho^* = -0.004$ a.u.) corresponds to the half of the isosurface in direction toward the side chain and the weaker one ($\rho^* = -0.003$ a.u.) to the other half. As this behavior is also observed in the NCI plots of $H^+PEA-Ar$ with $\rho^* = -0.003$ and -0.004 a.u., it is not caused by the F atom,

but results from the asymmetry in the interaction induced by the side chain.

In previous work,¹⁴ we compared the properties of the $oF-H^+PEA$ conformers with those of unsubstituted H^+PEA based on IRMPD spectra in the fingerprint range and B3LYP-D3 calculations. However, from the experimental point of view very little information on the effects of *ortho*-fluorination could

Table 3 Values of the electron density ρ^* for the minima of $s(\rho^*)$ marked in the NCI plots of $\text{H}^+\text{PEA}(\text{G})$, $\text{H}^+\text{PEA}(\text{G})-\text{Ar}(\text{i})$, $\text{oF-H}^+\text{PEA}(\text{Gf1})$, $\text{oF-H}^+\text{PEA}(\text{Gf1})-\text{Ar}(\text{i})$ in Fig. 4, including their assignments to noncovalent intra- and intermolecular interactions^a

Interaction	$\text{H}^+\text{PEA}(\text{G})^d$	$\text{H}^+\text{PEA}(\text{G})-\text{Ar}(\text{i})$	$\text{oF-H}^+\text{PEA}(\text{Gf1})^d$	$\text{oF-H}^+\text{PEA}(\text{Gf1})-\text{Ar}(\text{i})$
$\text{NH}^+\cdots\text{F}$			−0.013	−0.013
Phenyl ring closure	+0.024	+0.024	+0.024	+0.024
$\text{CNH}^+\cdots\text{FC}$ ring closure			+0.011/+0.008	+0.010/+0.008
$\text{NH}^+\cdots\pi^b$	−0.015/+0.016	±0.014	−0.010	−0.009
$\text{C}_\beta\text{H}\cdots\text{F}$			±0.011	±0.011
$\text{NH}^+\cdots\text{C}_5$			+0.009	+0.009
$\text{NH}^+\cdots\text{Ar}$		−0.008		−0.010
$\text{Ar}\cdots\pi^c$		−0.004/+0.003/+0.002		±0.003/±0.004

^a $\rho^* = \rho \text{ sign}(\lambda_2)$ in a.u.; attractive and repulsive interactions are characterized with a negative and positive sign. ^b This attractive interaction goes along with repulsive steric interactions of the side chain with the aromatic ring for $\text{H}^+\text{PEA}(\text{G})$. ^c Two minima corresponding to the weak $\text{Ar}\cdots\pi$ interaction indicated by the dashed gray line in the isosurface plot in Fig. 4c and d. ^d From ref. 14.

be obtained because the low-resolution IRMPD spectra of the $\text{oF-H}^+\text{PEA}$ and H^+PEA ions recorded at room temperature look quite similar, with the major exception of the additional CF stretch mode (σ_{CF}) of $\text{oF-H}^+\text{PEA}$ located at 1210 cm^{-1} and two bands assigned to aromatic CH bending modes. Hence, all information about the effects of site-specific aromatic fluorination on the noncovalent intramolecular bonds and the side chain conformation relied exclusively on the computations.¹⁴ In contrast, the comparison of the IRPD spectra of cold Rg-tagged $\text{oF-H}^+\text{PEA}$ and H^+PEA recorded in the NH stretch range reveals very different spectra (Fig. 2) providing invaluable experimental data on the effects of *ortho*-fluorination on the preferred side-chain conformation. The high-energy *anti* conformers of $\text{oF-H}^+\text{PEA}$ and H^+PEA have similar N–H bond properties, leading to essentially the same predicted IR spectra (to within 1 cm^{-1}). However, the most stable G conformer of H^+PEA differs drastically from the corresponding Gh conformer of $\text{oF-H}^+\text{PEA}$. The $\text{NH}^+\cdots\pi$ interaction in $\text{H}^+\text{PEA}(\text{G})$ is stronger ($R_{\text{NH}\cdots\pi} = 2.93 \text{ \AA}$ and $\rho^* = -0.015 \text{ a.u.}$) than in $\text{oF-H}^+\text{PEA}(\text{Gh})$ ($R_{\text{NH}\cdots\pi} = 3.02 \text{ \AA}$ and $\rho^* = -0.014 \text{ a.u.}$), leading to a lower bound NH stretch frequency ($\nu^b = 3164 \text{ versus } 3201 \text{ cm}^{-1}$). Thus, in contrast to H^+PEA , for which the G conformer is the global minimum and the only conformer detected experimentally, *ortho*-fluorination destabilizes the Gh conformer such that it is only a higher-energy conformer and experimentally not detected. Instead, the two lowest-energy Gf1 and Gf2 conformers of $\text{oF-H}^+\text{PEA}$, which are indeed experimentally observed, are stabilized by $\text{NH}^+\cdots\text{F}$ interactions, which of course are absent in H^+PEA . The minor Gf2 conformer has a very strong $\text{NH}^+\cdots\text{F}$ interaction but no $\text{NH}^+\cdots\pi$ contact, while the most abundant and energetically most stable Gf1 conformer is stabilized by $\text{NH}^+\cdots\pi$ and $\text{NH}^+\cdots\text{F}$ contacts of medium strength. This spectral comparison demonstrates that *ortho*-fluorination drastically changes the noncovalent interactions in this prototypical protonated neurotransmitter, leading to the detection of completely different conformers in the NH stretch range, which is a very sensitive probe of these noncovalent intramolecular bonds. For example, the band D in the $\text{oF-H}^+\text{PEA}-\text{Ar}$ spectrum at 3122 cm^{-1} is characteristic of the strong $\text{NH}^+\cdots\text{F}$ interaction of the Gf2 conformer, and occurs close to band C in the $\text{H}^+\text{PEA}-\text{Ar}$ spectrum at 3123 cm^{-1} , which is characteristic for the strong $\text{NH}^+\cdots\pi$ interaction of the G conformer. This coincidence suggests that

the two different types of noncovalent interactions in these two different conformers have similar strengths.

4. Concluding remarks

The drastic impact of $\text{H} \rightarrow \text{F}$ substitution on the inter- and intramolecular noncovalent forces of the *ortho*-fluorinated protonated prototypical neurotransmitter $\text{oF-H}^+\text{PEA}$ is characterized by IRPD spectroscopy of cold ions in the NH stretch range using Rg tagging with Ne and Ar and quantum chemical calculations at the dispersion-corrected B3LYP-D3/aug-cc-pVTZ level. These IRPD spectra provide the first experimental information on the strength of the competing noncovalent $\text{NH}^+\cdots\pi$ and $\text{NH}^+\cdots\text{F}$ interaction motifs, which change upon site-specific aromatic fluorination. In contrast to previous low-resolution IRMPD spectra of room-temperature ions in the fingerprint range, the higher-resolution IRPD spectra of cold $\text{oF-H}^+\text{PEA}-\text{Rg}$ dimers in the NH stretch range are able to distinguish between the three low-energy *gauche* conformers of $\text{oF-H}^+\text{PEA}$. The analysis of the conformation-sensitive NH stretch spectra clearly shows the predominant population of the most stable Gf1 conformer, which is stabilized by both $\text{NH}^+\cdots\pi$ and $\text{NH}^+\cdots\text{F}$ contacts of medium strength. The slightly less stable Gf2 conformer, which lacks any $\text{NH}^+\cdots\pi$ interaction, is strongly stabilized by the substantial $\text{NH}^+\cdots\text{F}$ interaction and detected as a minor population in the molecular beam ($\sim 5\%$). The Gh conformer of $\text{oF-H}^+\text{PEA}$, which is only stabilized by a $\text{NH}^+\cdots\pi$ interaction, is the least stable *gauche* conformer and not detected experimentally. This is in contrast to the related G conformer of H^+PEA , which is the global minimum and the only conformer detected for the unsubstituted ion. The NCI calculations provide a quantitative analysis of the competing noncovalent intermolecular and intramolecular interactions, which can be of comparable strength for the Ar-tagged $\text{oF-H}^+\text{PEA}$ ions. The Rg ligand prefers a binding site at which it maximizes the dispersive interaction with the aromatic π electron system and charge-induced dipole interaction with the ammonium group. Although the intermolecular interactions with the Rg atoms can compete with the noncovalent intramolecular bonds, they induce only minor spectral shifts in the NH stretch range. In the future, it may be interesting to

characterize $x\text{F-H}^+\text{PEA-(H}_2\text{O)}_n$ clusters using the same experimental and computational approach in order to probe the effects of site-specific aromatic fluorination on the structure of the micro-hydration network around this prototypical protonated neurotransmitter under more realistic physiological conditions.^{16,41–48}

Acknowledgements

This work was supported by Deutsche Forschungsgemeinschaft (DFG, DO 729/3) and the German-Israeli Foundation for Scientific Research and Development (GIF, 1164-158.5/2011). A. B. has received funding from the People Programme (Marie Curie Actions) of the European Union's Seventh Framework Programme (FP7/2007-2013) under REA grant agreement no. 600209 (TU Berlin/IPODI). We thank S. Melandri, I. Bar, and S. Fornarini for stimulating discussions.

References

- 1 B. K. Park, N. R. Kitteringham and P. M. O'Neill, *Annu. Rev. Pharmacol. Toxicol.*, 2001, **41**, 443–470.
- 2 H.-J. Böhm, D. Banner, S. Bendels, M. Kansy, B. Kuhn, K. Müller, U. Obst-Sander and M. Stahl, *ChemBioChem*, 2004, **5**, 637–643.
- 3 C. Isanbor and D. O'Hagan, *J. Fluorine Chem.*, 2006, **127**, 303–319.
- 4 J.-P. Bégue and D. Bonnet-Delpon, *J. Fluorine Chem.*, 2006, **127**, 992–1012.
- 5 K. L. Kirk, *J. Fluorine Chem.*, 2006, **127**, 1013–1029.
- 6 K. Müller, C. Faeh and F. Diederich, *Science*, 2007, **317**, 1881–1886.
- 7 S. Purser, P. R. Moore, S. Swallow and V. Gouverneur, *Chem. Soc. Rev.*, 2008, **37**, 320–330.
- 8 W. K. Hagmann, *J. Med. Chem.*, 2008, **51**, 4359–4369.
- 9 D. O'Hagan, *J. Fluorine Chem.*, 2010, **131**, 1071–1081.
- 10 A. Lagutschenkov, J. Langer, G. Berden, J. Oomens and O. Dopfer, *J. Phys. Chem. A*, 2010, **114**, 13268–13276.
- 11 A. Lagutschenkov, J. Langer, G. Berden, J. Oomens and O. Dopfer, *Phys. Chem. Chem. Phys.*, 2011, **13**, 15644–15656.
- 12 A. Lagutschenkov, J. Langer, G. Berden, J. Oomens and O. Dopfer, *Phys. Chem. Chem. Phys.*, 2011, **13**, 2815–2823.
- 13 B. Chiavarino, M. E. Crestoni, M. Schütz, A. Bouchet, S. Piccirillo, V. Steinmetz, O. Dopfer and S. Fornarini, *J. Phys. Chem. A*, 2014, **118**, 7130–7138.
- 14 M. Schütz, A. Bouchet, B. Chiavarino, M. E. Crestoni, S. Fornarini and O. Dopfer, *Chem. – Eur. J.*, 2016, **22**, 8124–8136.
- 15 A. Bouchet, M. Schütz, B. Chiavarino, M. E. Crestoni, S. Fornarini and O. Dopfer, *Phys. Chem. Chem. Phys.*, 2015, **17**, 25742–25754.
- 16 A. Bouchet, M. Schütz and O. Dopfer, *ChemPhysChem*, 2016, **17**, 232–243.
- 17 M. Okumura, L. I. Yeh and Y. T. Lee, *J. Chem. Phys.*, 1988, **88**, 79–91.
- 18 M. Okumura, L. I. Yeh, J. D. Myers and Y. T. Lee, *J. Phys. Chem.*, 1990, **94**, 3416–3427.
- 19 M. A. Duncan, *Int. J. Mass Spectrom.*, 2000, **200**, 545–569.
- 20 M. A. Duncan, *J. Phys. Chem. A*, 2012, **116**, 11477–11491.
- 21 E. J. Bieske and O. Dopfer, *Chem. Rev.*, 2000, **100**, 3963–3998.
- 22 O. Dopfer, *Z. Phys. Chem.*, 2005, **219**, 125–168.
- 23 A. Patzer, M. Schütz, T. Möller and O. Dopfer, *Angew. Chem., Int. Ed.*, 2012, **51**, 4925–4929.
- 24 M. Savoca, J. Langer and O. Dopfer, *Angew. Chem., Int. Ed.*, 2013, **52**, 1568–1571.
- 25 N. Solcà and O. Dopfer, *Angew. Chem., Int. Ed.*, 2002, **41**, 3628–3631.
- 26 H.-S. Andrei, N. Solcà and O. Dopfer, *Angew. Chem., Int. Ed.*, 2008, **47**, 395–397.
- 27 A. Patzer, S. Chakraborty, N. Solcà and O. Dopfer, *Angew. Chem., Int. Ed.*, 2010, **49**, 10145–10148.
- 28 G. Féraud, M. Broquier, C. Dedonder-Lardeux, G. Grégoire, S. Soorkia and C. Juvet, *Phys. Chem. Chem. Phys.*, 2014, **16**, 5250–5259.
- 29 J. C. López, V. Cortijo, S. Blanco and J. L. Alonso, *Phys. Chem. Chem. Phys.*, 2007, **9**, 4521–4527.
- 30 A. Golan, N. Mayorkas, S. Rosenwaks and I. Bar, *J. Chem. Phys.*, 2009, **131**, 24305.
- 31 S. Melandri, A. Merloni and A. Maris, *ChemPhysChem*, 2012, **13**, 3504–3509.
- 32 N. Mayorkas, H. Sachs, M. Schütz, S. Ishiuchi, M. Fujii, O. Dopfer and I. Bar, *Phys. Chem. Chem. Phys.*, 2016, **18**, 1191–1201.
- 33 O. Dopfer, *Int. Rev. Phys. Chem.*, 2003, **22**, 437–495.
- 34 M. J. Frisch, G. W. Trucks, H. B. Schlegel, G. E. Scuseria, M. A. Robb, J. R. Cheeseman, G. Scalmani, V. Barone, B. Mennucci, G. A. Petersson, H. Nakatsuji, M. Caricato, X. Li, H. P. Hratchian, A. F. Izmaylov, J. Bloino, G. Zheng, J. L. Sonnenberg, M. Hada, M. Ehara, K. Toyota, R. Fukuda, J. Hasegawa, M. Ishida, T. Nakajima, Y. Honda, O. Kitao, H. Nakai, T. Vreven, J. A. Montgomery Jr., J. E. Peralta, F. Ogliaro, M. Bearpark, J. J. Heyd, E. Brothers, K. N. Kudin, V. N. Staroverov, R. Kobayashi, J. Normand, K. Raghavachari, A. Rendell, J. C. Burant, S. S. Iyengar, J. Tomasi, M. Cossi, N. Rega, J. M. Millam, M. Klene, J. E. Knox, J. B. Cross, V. Bakken, C. Adamo, J. Jaramillo, R. Gomperts, R. E. Stratmann, O. Yazyev, A. J. Austin, R. Cammi, C. Pomelli, J. W. Ochterski, R. L. Martin, K. Morokuma, V. G. Zakrzewski, G. A. Voth, P. Salvador, J. J. Dannenberg, S. Dapprich, A. D. Daniels, Ö. Farkas, J. B. Foresman, J. V. Ortiz, J. Cioslowski and D. J. Fox, *Gaussian 09, Revision D.01*, Gaussian, Inc., Wallingford CT, 2009.
- 35 E. D. Glendening, A. E. Reed, J. E. Carpenter and F. Weinhold, *NBO 3.1*, Theoretical Chemistry Institute, University of Wisconsin, Madison, 2013.
- 36 E. R. Johnson, S. Keinan, P. Mori-Sánchez, J. Contreras-García, A. J. Cohen and W. Yang, *J. Am. Chem. Soc.*, 2010, **132**, 6498–6506.
- 37 J. Contreras-García, E. R. Johnson, S. Keinan, R. Chaudret, J. P. Piquemal, D. N. Beratan and W. Yang, *J. Chem. Theory Comput.*, 2011, **7**, 625–632.

- 38 O. Dopfer, S. A. Nizkorodov, M. Meuwly, E. J. Bieske and J. P. Maier, *Int. J. Mass Spectrom. Ion Processes*, 1997, **167–168**, 637–647.
- 39 N. M. Lakin, R. V. Olkhov and O. Dopfer, *Faraday Discuss.*, 2001, **118**, 455–476.
- 40 E. J. Bieske, S. A. Nizkorodov, O. Dopfer, J. P. Maier, R. J. Stickland, B. J. Cotterell and B. J. Howard, *Chem. Phys. Lett.*, 1996, **250**, 266–272.
- 41 M. Schütz, K. Sakota, R. Moritz, M. Schmies, T. Ikeda, H. Sekiya and O. Dopfer, *J. Phys. Chem. A*, 2015, **119**, 10035–10051.
- 42 J. Klyne, M. Schmies, M. Fujii and O. Dopfer, *J. Phys. Chem. B*, 2015, **119**, 1388–1406.
- 43 M. Schmies, M. Miyazaki, M. Fujii and O. Dopfer, *J. Chem. Phys.*, 2014, **141**, 214301.
- 44 O. Dopfer, A. Patzer, S. Chakraborty, I. Alata, R. Omidyan, M. Broquier, C. Dedonder and C. Jouvét, *J. Chem. Phys.*, 2014, **140**, 124314.
- 45 S. Chakraborty, A. Patzer, A. Lagutschenkov, J. Langer and O. Dopfer, *Chem. Phys. Lett.*, 2010, **485**, 49–55.
- 46 H. Andrei, N. Solcà and O. Dopfer, *ChemPhysChem*, 2006, **7**, 107–110.
- 47 A. A. Adesokan, G. M. Chaban, O. Dopfer and R. B. Gerber, *J. Phys. Chem. A*, 2007, **111**, 7374–7381.
- 48 N. Solcà and O. Dopfer, *J. Phys. Chem. A*, 2003, **107**, 4046–4055.